JOURNAL OF AIRCRAFT
Vol. 47, No. 4, July–August 2010

Numerical Simulation of Rotor Using Coupled Computational Fluid Dynamics and Free Wake

Seong Yong Wie,* Dong Kyun Im,† Jang Hyuk Kwon,‡ and Duck Joo Lee§
Korea Advanced Institute of Science and Technology, Daejeon 305-701, Republic of Korea

DOI: 10.2514/1.46797

Rotor aerodynamics is governed by wake behavior. Particularly, aerodynamic performance in the hovering flight condition is determined by the structure and the strength of the wake. In this paper, rotating blades were simulated using a tightly coupled computational fluid dynamics and time-marching free-wake method in hovering and forward flight. The rotating blades and a flowfield near the rotor are calculated by the computational fluid dynamics, and the strength and motions of the wake are simulated with the time-marching free-wake method. A moving overset grid technique is applied to consider rotor motions during hovering and forward flight. Inflow and outflow conditions in the computational fluid dynamics domain are provided from an induced flow rate by the time-marching free-wake method at each time step. The strength of the trailed vortices is determined from a sectional lift calculated in the rotating blade, which is computed using the computational fluid dynamics. The present coupled method was compared with other inflow and outflow conditions, such as source–sink and Riemann-invariant conditions. To investigate the robustness of the present method, grid-size effects were also tested in large and small background grid systems.

Nomenclature

a	=	distance between velocity position and vortex filament
a_c	=	vortex core radius
a_∞	=	speed of sound
C_p	=	pressure coefficient
C_T	=	rotor thrust coefficient, thrust$/[\pi\rho_\infty R^3(\Omega R)^2]$
c	=	blade chord length
M_{Tip}	=	tip Mach number, $\Omega R/a_\infty$
R	=	rotor radius
r	=	spanwise distance along rotor
$\mathbf{y}$	=	wake node position
β	=	flapping angle
Γ	=	vortex circulation strength
Γ_{bound}	=	bound vortex circulation strength
Γ_{trailed}	=	trailed vortex circulation strength
θ	=	pitch angle
ψ	=	azimuth angle

I. Introduction

GENERALLY, wake description is the most important factor in rotor aerodynamic predictions, because a downwash induced by the wake changes a rotor's performance. If the rotor wake is well simulated, then aerodynamic characteristics of the rotor can be accurately predicted. However, the wake characteristics are not clearly described due to a numerical dissipation in the rotor computational fluid dynamics (CFD) calculation. This dissipation problem causes a diminishing flow vorticity in the rotor wake. The numerically diminished wake cannot create sufficient induced velocity and inflow to describe the rotor aerodynamic performance.

Received 20 August 2009; revision received 14 December 2009; accepted for publication 21 December 2009.

*Ph.D. Candidate, School of Mechanical, Aerospace, and Systems Engineering; wsy278@kaist.ac.kr.
†Ph.D. Candidate, School of Mechanical, Aerospace, and Systems Engineering; poong04@kaist.ac.kr.
‡Professor, School of Mechanical, Aerospace, and Systems Engineering; jhkwon@kaist.ac.kr. Member AIAA.
§Professor, School of Mechanical, Aerospace, and Systems Engineering; djlee@kaist.ac.kr. Member AIAA.

Rotor noise, as well as the rotor aerodynamic performance, depends on the rotor wake's behavior. Specifically, an interaction between the wake and the rotating blades generates an unsteady aerodynamic instability and noise. In slow descending and maneuvering flight conditions, the tip vortex and the wake directly interact with the blades and the fuselage. For these specific flight conditions, the tip vortex and the wake bring serious aerodynamic instability and noise.

For this reason, many numerical methods have been developed and applied to describe the behavior of the wake. In the rotor CFD, adapted grid methods and high-order numerical methods [1] have been developed to reduce numerical dissipation of vortical flowfield. The adapted grid technique is commonly used to reduce numerical

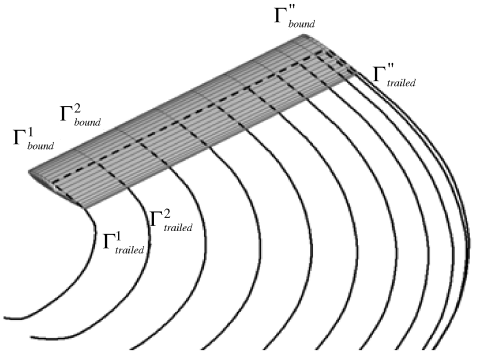

Fig. 1 Schematic of trailed and bound vortices.

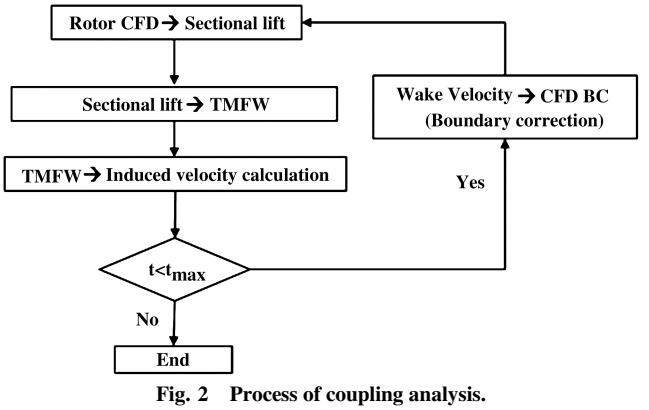

Fig. 2 Process of coupling analysis.

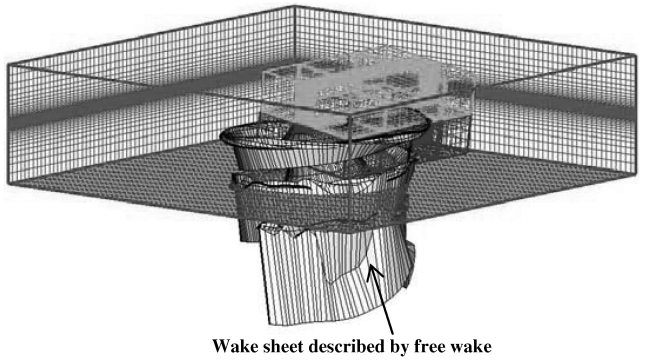

Fig. 3 Wake sheet in the CFD domain.

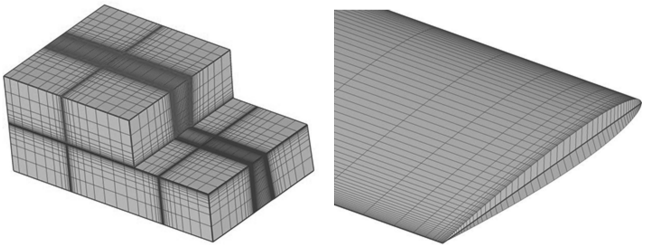

Fig. 4 Blade grid.

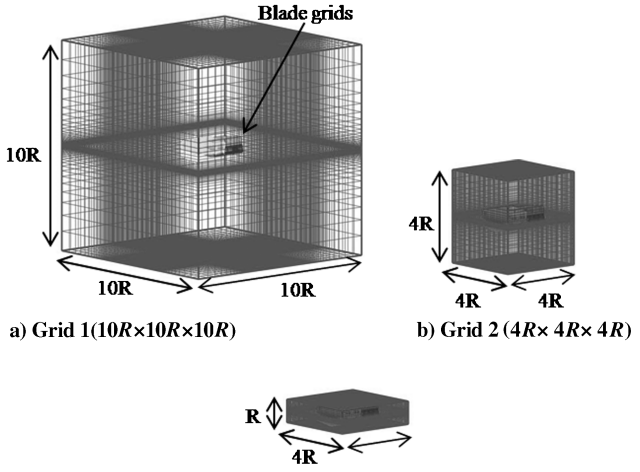

a) Grid 1(10*R*×10*R*×10*R*) **b) Grid 2 (4*R*× 4*R*× 4*R*)**

c) Grid 3 (4*R*× 4*R*× *R*)

Fig. 5 Background grid and blade grids: a) grid 1, b) grid 2, and c) grid 3.

dissipation. Lately, a vortex-adapted grid using a chimera technique [2] has been applied to conserve tip vortices of the rotor in forward flight. These high-order schemes were also used to avoid dissipation problems.

With recent improvements of the rotor CFD method, the advanced vortex methods (such as the vortex particle method [3] and the vortex transport method [4]) have been developed to describe wake convection. These vortex methods are very powerful in the incompressible flowfield. Tip vortices and the wake of the rotor are implemented clearly without numerical dissipation. In particular, aerodynamic unsteadiness and wake motion can be simulated when a body is submerged in the wake. However, these vortex methods have

Table 1 Thrust coefficient ($M_{\text{Tip}} = 0.439$)[a]

Background grid	Present	Source–sink	Riemann invariant
Grid 1: $10 \times 10 \times 10R$	0.00494	0.00496	0.00498
Grid 2: $4 \times 4 \times 4R$	0.00494	0.00516	0.00504
Grid 3: $4 \times 4 \times 4R$	0.00492	0.00562	0.00622

[a](Experiment $C_T = 0.00459$)

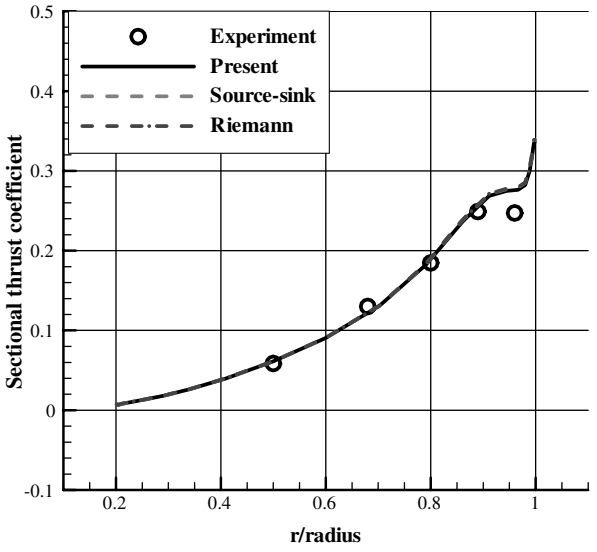

a) Grid 1 (10*R* × 10*R* × 10*R*)

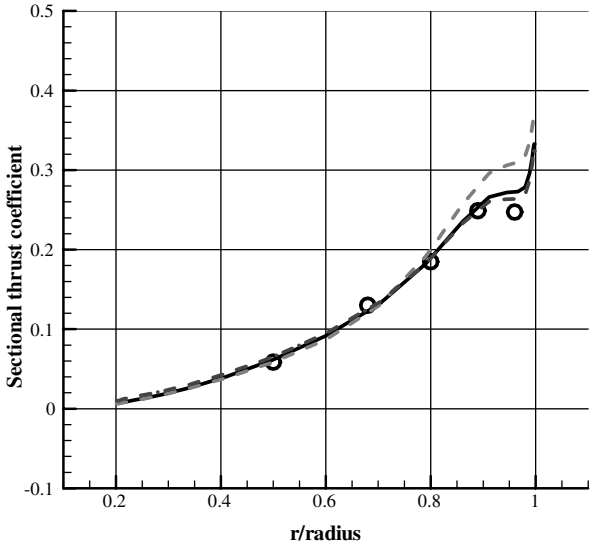

b) Grid 2 (4*R* × 4*R* × 4*R*)

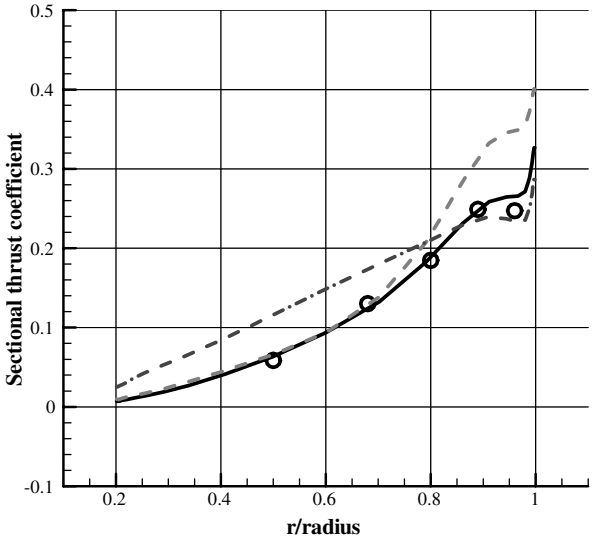

c) Grid 3 (4*R* × 4*R* × *R*)

Fig. 6 Sectional thrust coefficients ($M_{\text{Tip}} = 0.439$).

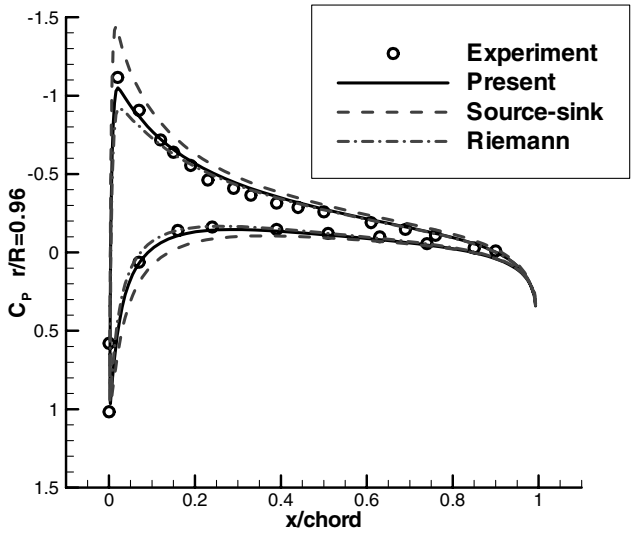

a) r/R=0.96

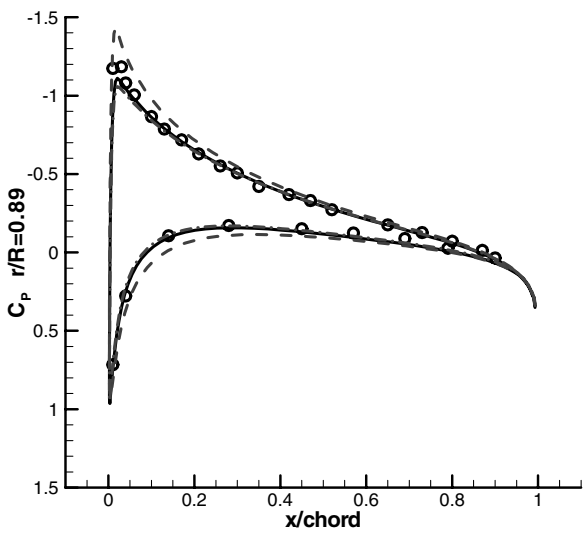

b) r/R=0.89

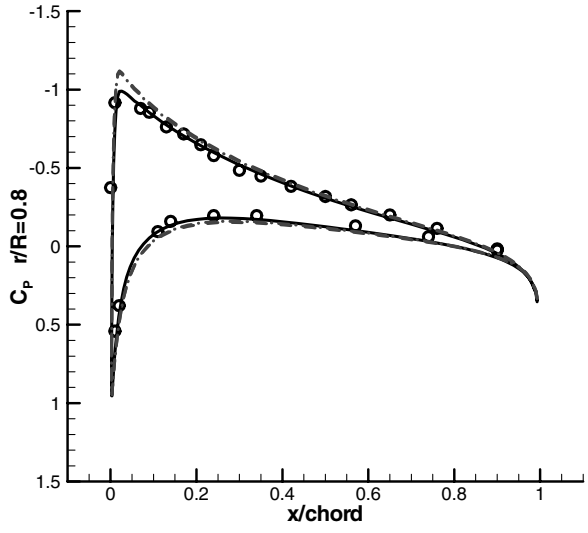

c) r/R=0.8

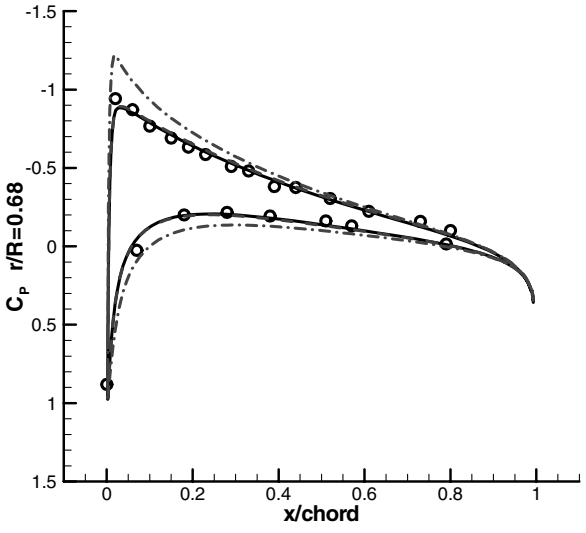

d) r/R=0.68

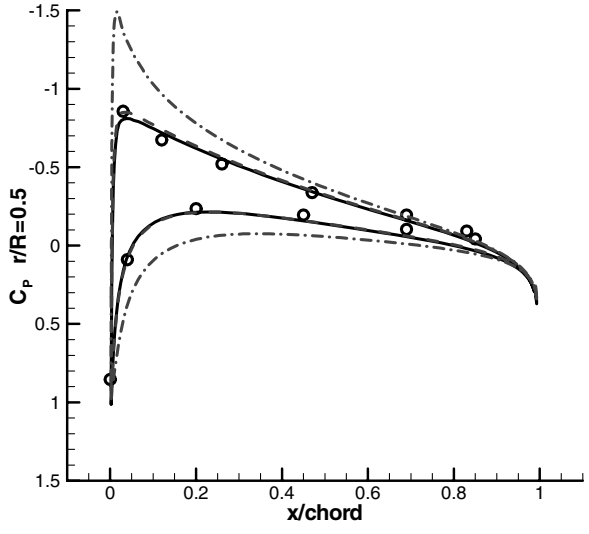

e) r/R=0.5

Fig. 7 Pressure coefficients (grid 3, $M_{\text{Tip}} = 0.439$).

difficulty simulating the rotor aerodynamics, including shock problems in the high tip Mach number.

Coupling analysis has also been used for rotor aerodynamics and wake simulation. Berkman and Sankar [5] used tip vortices described by free wake in a potential domain coupled with the Navier–Stokes solver. Using a tip vortex model, an inflow from far field was described. However, this model only considered the tip vortex without an inboard vortex sheet.

The vortex sheet of the prescribed wake was also coupled with CFD for an efficient and accurate simulation [6]. In this coupling analysis, a steady analysis was studied and a rigid wake model was applied for describing the wake of the rotating blades. This method effectively predicted rotor performance, but it cannot be used in forward and unsteady motion due to its rigid wake model.

In this paper, a tightly coupled CFD/time-marching free-wake (TMFW) method is presented for accurate and efficient rotor aerodynamics prediction of hovering and forwarding flight. The present TMFW is directly connected with the blade trailing edge in the CFD domain. The coupling analysis can be used in both the unsteady and steady states. Because the inboard wake sheet, as well as the tip vortex, would be considered during the entire set of computations, it is more realistic and reasonable than the conventional coupling analysis.

Generally, conventional coupling methods have used the velocity field approach, which considers induced velocity of the rotor wake at all node points in the computational domain. This velocity field approach requires a large number of calculations. However, the present coupling method uses the boundary correction approach. In the boundary correction approach, induced velocity at the boundary surface of the computational domain is computed by the rotor wake sheet of the free wake. The computed induced velocity can provide an accurate boundary condition. It is more efficient than the velocity field approach in the unsteady flight condition.

Induced velocity at the boundary means inflow and outflow. For that reason, hovering flight simulation can be effectively performed, because the free-wake analysis supports inflow and outflow conditions in the rotor CFD. To investigate wake effect in detail, the present coupling analysis was compared with the conventional rotor CFD approach. In addition, forward flight with blade motion was also simulated using the present coupling method.

II. Numerical Methods

A. Numerical Schemes

The three-dimensional unsteady Euler equation is a governing equation:

$$\frac{\partial \mathbf{Q}}{\partial t} + \frac{\partial \mathbf{F}}{\partial x} + \frac{\partial \mathbf{G}}{\partial y} + \frac{\partial \mathbf{H}}{\partial z} = 0 \tag{1}$$

where

$$\mathbf{Q} = [\rho,\ \rho u,\ \rho v,\ \rho w,\ \rho E]$$

$$\mathbf{F} = [\rho u,\ \rho u^2 + p,\ \rho uv,\ \rho uw,\ \rho uE + pu]$$

$$\mathbf{G} = [\rho v,\ \rho uv,\ \rho v^2 + p,\ \rho vw,\ \rho vE + pv]$$

$$\mathbf{H} = [\rho w,\ \rho uw,\ \rho vw,\ \rho w^2 + p,\ \rho wE + pw]$$

$$E = \frac{p}{(\gamma - 1)\rho} + \frac{1}{2}V^2$$

Table 2 Thrust coefficient ($M_{\text{Tip}} = 0.877$)[a]

Background grid	Present	Source–sink	Riemann invariant
Grid 1: $10 \times 10 \times 10R$	0.00553	0.00554	0.00556
Grid 2: $4 \times 4 \times 4R$	0.00560	0.00576	0.00568
Grid 3: $4 \times 4 \times 4R$	0.00549	0.00606	0.00718

[a](Experiment $C_T = 0.00477$)

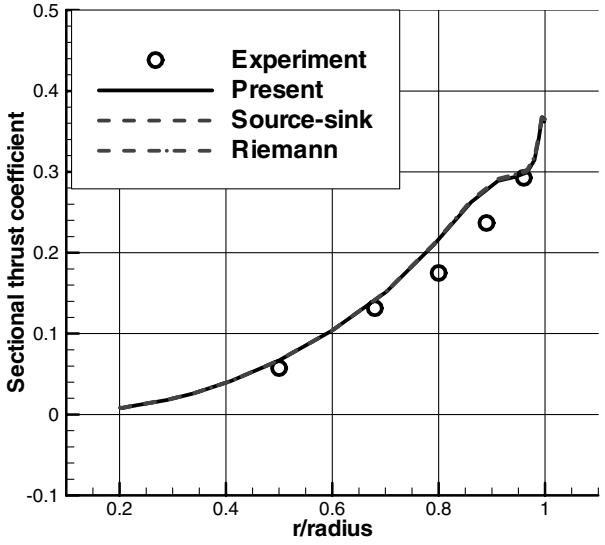

a) Grid 1 ($10R \times 10R \times 10R$)

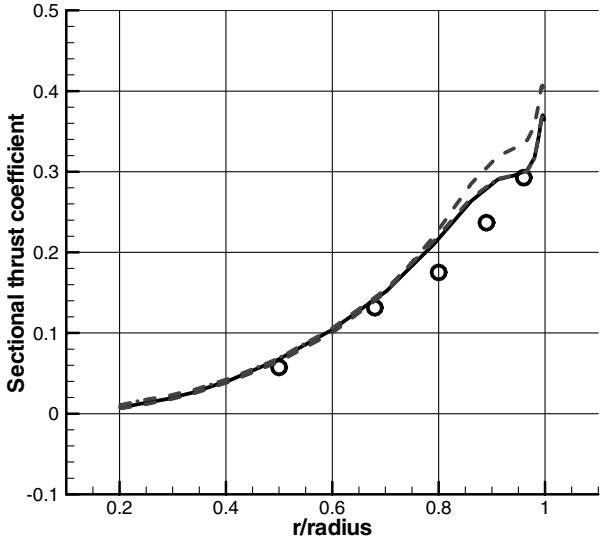

b) Grid 2 ($4R \times 4R \times 4R$)

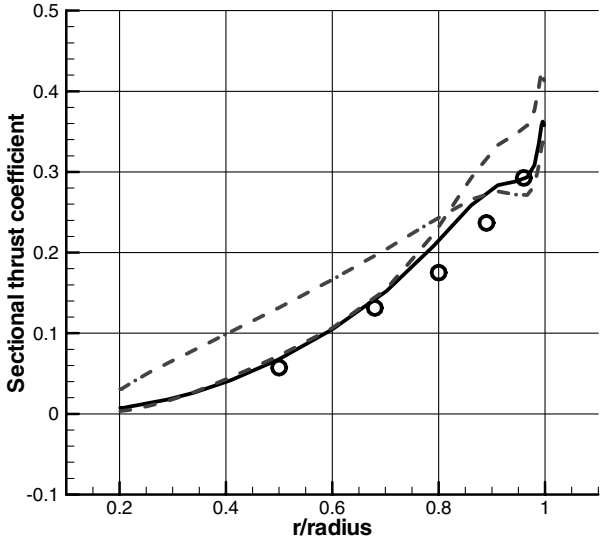

c) Grid 3 ($4R \times 4R \times R$)

Fig. 8 Sectional thrust coefficients ($M_{\text{Tip}} = 0.877$).

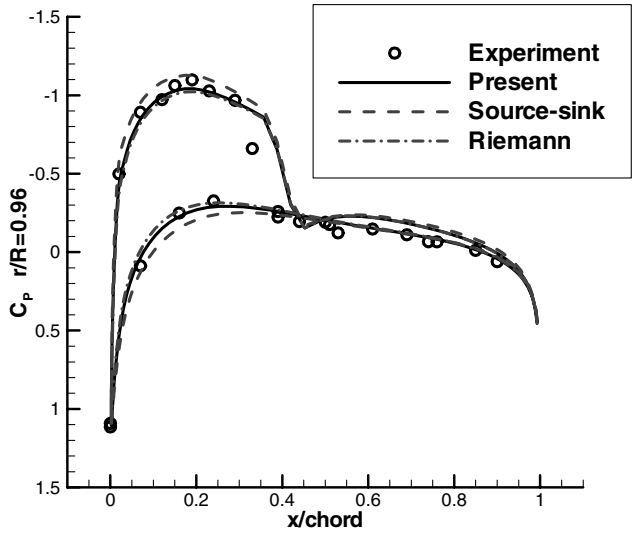

a) r/R=0.96

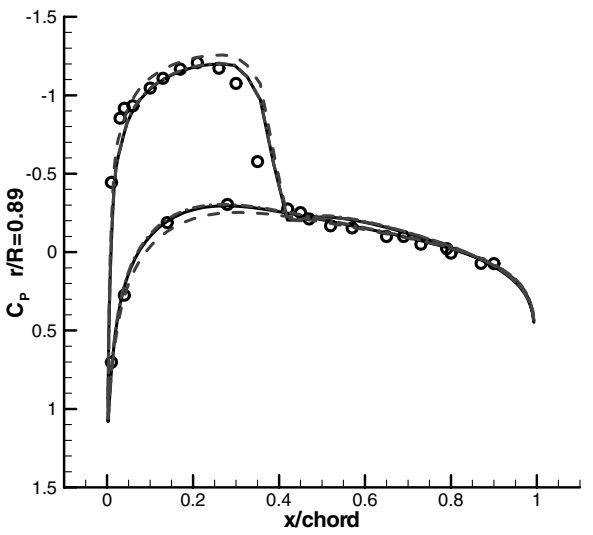

b) r/R=0.89

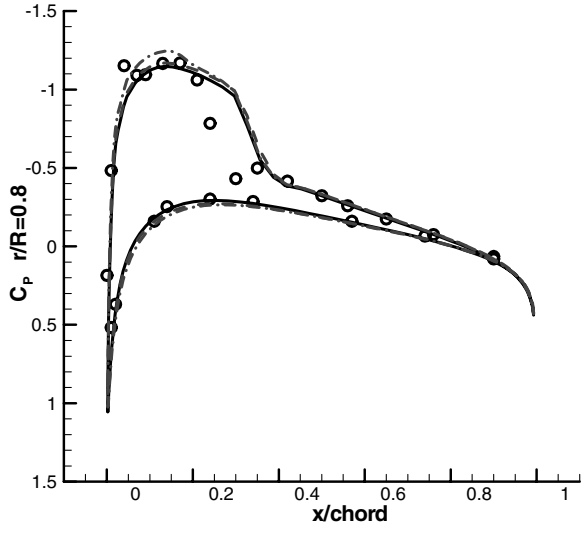

c) r/R=0.8

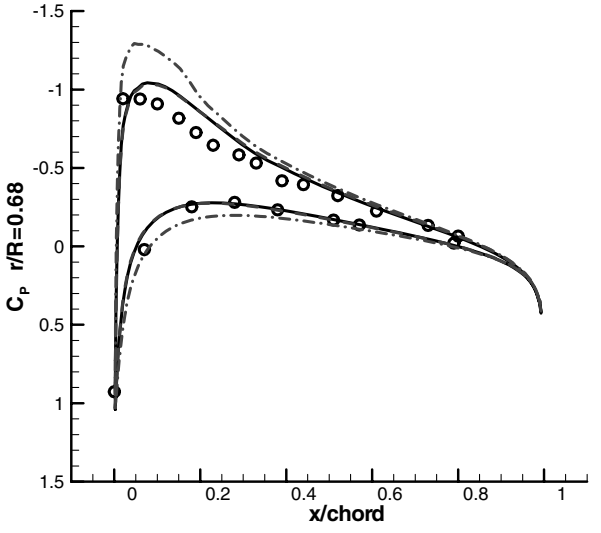

d) r/R=0.68

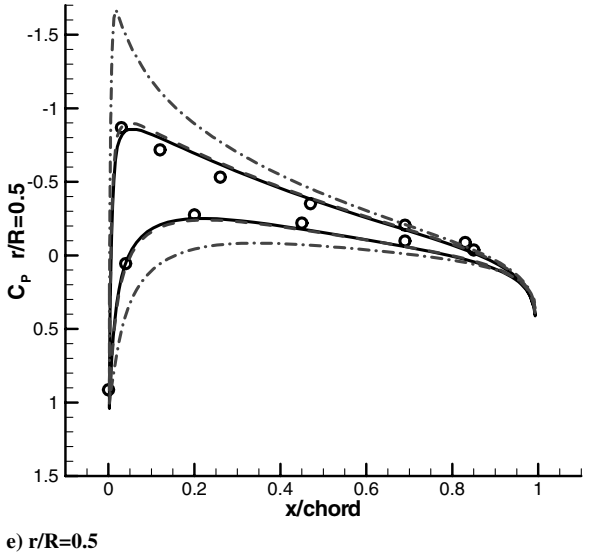

e) r/R=0.5

Fig. 9 Pressure coefficients (grid 3, $M_{\text{Tip}} = 0.877$).

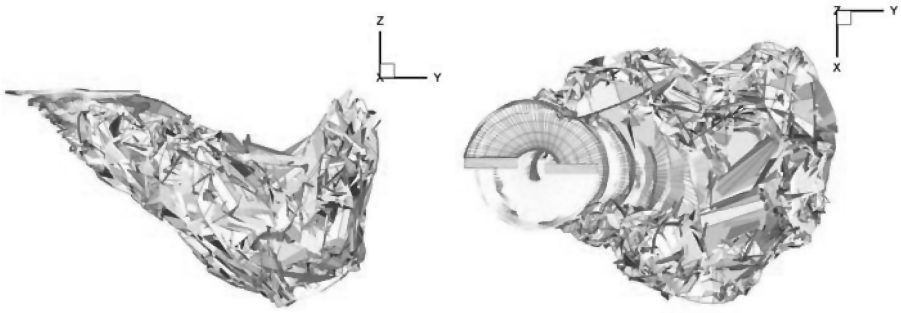

Fig. 10 Wake structure ($M_{\text{Tip}} = 0.439$, $\mu = 0.05$).

The finite-volume method (FVM) is used to discretize the governing equation. In this FVM, the cell-centered method is used. Third-order MUSCL is used and a van Leer limiter using Roe's flux difference splitting and the Harten–Yee entropy fix function is applied [7–9]. Time integration to a steady state is accomplished with a diagonalized alternating-direction-implicit scheme, and to increase time accuracy, a dual time-stepping method is applied for an unsteady state [10,11]. The boundary inflow/outflow conditions were determined by coupling with a free wake.

B. Overset Grid and Parallel Computation

The overset grid method is used to describe the rotor blade, which is separated from some subgrids, to the independent grid system for each subgrid. The independent grids transfer information of each subgrid through an interpolation point by the domain connectivity method. This study used a modified overset grid technique for robustness and accuracy of flow analysis by arranging the interpolation points of overlapped grids away from the boundary of a multi-subgrid [12].

A structured grid assembly is parallelized using a static load balancing tied to the flow solver, based on the grid size of a decomposed domain. The parallel algorithm is modified for a distributed memory system. To parallelize the grid assembly, a message-passing programming model based on the message-passing interface library is implemented using the SPMD (single-program multiple-data) paradigm. The parallelized flow solver can be executed in each processor with the static load balancing by the preprocessor.

C. Conventional Inflow/Outflow Conditions

Inflow and outflow conditions in the far field are very crucial to predict the rotor performance. In particular, the capability of a hovering simulation is dependent on the inflow rate due to the hovering wake structure. In hovering flight, the inflow rate induced from the wake is usually obtained from a source–sink model based on one-dimensional momentum theory [13,14]:

outflow:

$$W_e = -2M_{\text{Tip}}\sqrt{\frac{C_T}{2}} \tag{2}$$

inflow:

$$W_r = -(M_{\text{Tip}}/4)\sqrt{\frac{C_T}{2}}\left(\frac{R}{r}\right)^2 \tag{3}$$

where W_e is the outflow rate and W_r is the inflow rate. The inflow/outflow rates are determined by the thrust coefficient C_T, the rotor radius R, the tip Mach number M_{Tip}, and the distance from the rotation origin r.

In the opening condition, the characteristic boundary condition can also be used for inflow and outflow.

Riemann invariant:

$$R_o = U_o - \frac{2a_{\infty,o}}{\gamma - 1}; \qquad R_i = U_i + \frac{2a_{\infty,i}}{\gamma - 1} \tag{4}$$

where the subindices o and i denote the outflow and inflow properties. U indicates normal velocity at the boundary. The ratio of specific heat is γ. The Inflow and outflow properties at the far field are determined by the Riemann-invariant method.

III. Time-Marching Free-Wake Coupling for Unsteady Aerodynamics

Generally, an inflow condition of a hovering simulation uses the source–sink model. It is based on the one-dimensional momentum theory, which is derived from the fully developed flow. For that reason, it has a limitation in the rotor simulation of unsteady motions, such as the coaxial rotor, slow forward, and maneuvering motions. In the present study, the inflow variation induced by the wake of the rotating blades is decided by a free-wake routine. It is more general than the conventional inflow and outflow boundary conditions.

A. Free-Wake Model

The wake is described as vortex filaments. Induced velocity of the vortex filament can be obtained from the Biot–Savart law, which is shown next:

$$d\mathbf{V} = \frac{\Gamma}{4\pi}\frac{d\boldsymbol{l} \times \mathbf{a}}{|\mathbf{a}|^3} \tag{5}$$

where $d\boldsymbol{l}$ is the vortex filament length, $\mathbf{a}$ is a distance between the velocity position and the vortex filament, and Γ is the vortex strength. From Eq. (5), we see that a singularity occurs at $\mathbf{a} = 0$. To avoid this singularity problem, a vortex model is used. In this study, Vatistas et al.'s vortex model [15] is applied. This model is commonly used in a vortex method. The core size in the model is 0.1 chord, which is correlated with other mathematical and experimental investigations [16].

Vatistas et al.'s vortex model [15]:

$$v_\theta = \frac{\Gamma}{2\pi r_c}\frac{\mathbf{a}/\mathbf{a}_c}{\sqrt{1 + (\mathbf{a}/\mathbf{a}_c)^4}}; \qquad a_c\text{: vortex core radius} \tag{6}$$

A high-order scheme for the time integration can be used to predict an accurate wake position, which is necessary for the performance prediction. In the present study, a fourth-order Adams–Bashforth–Moulton method [17] is applied for the time integration. This is a predictor–corrector method. This method has been known to be more stable than a conventional explicit method for the wake convection. The fourth-order Adams–Bashforth–Moulton method is given as

Table 3 Average thrust coefficient ($M_{\text{Tip}} = 0.439$, $\mu = 0.05$)

Condition: grid	Average C_T
Present: 3	0.00556
Riemann: 1	0.00567
Riemann: 2	0.00583
Riemann: 3	0.00687

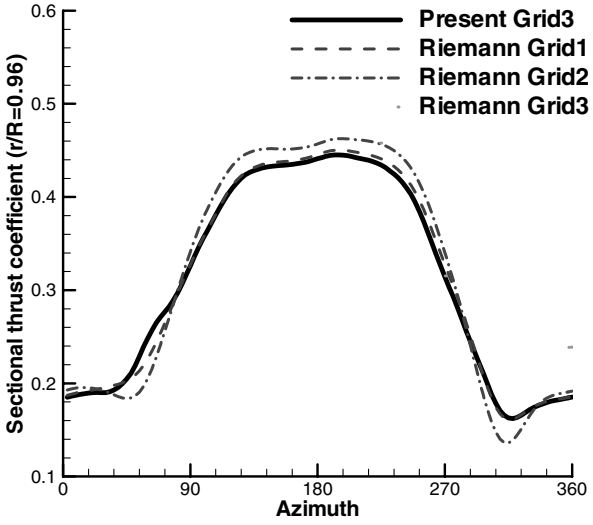

a) r/R=0.96

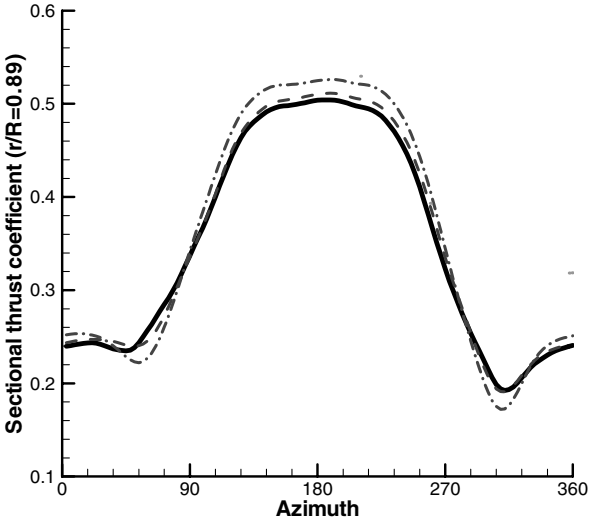

b) r/R=0.89

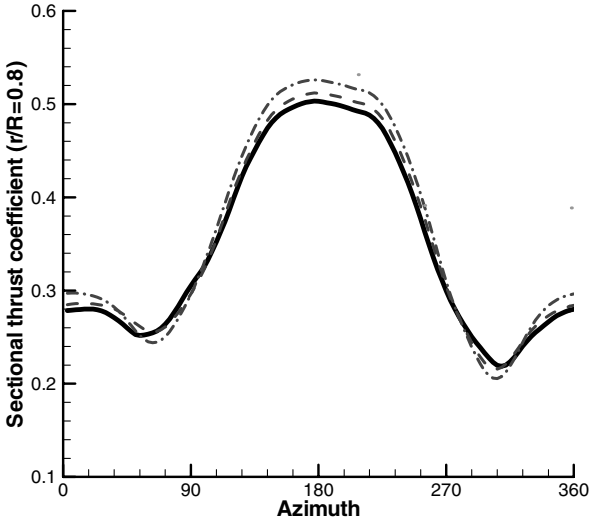

c) r/R=0.8

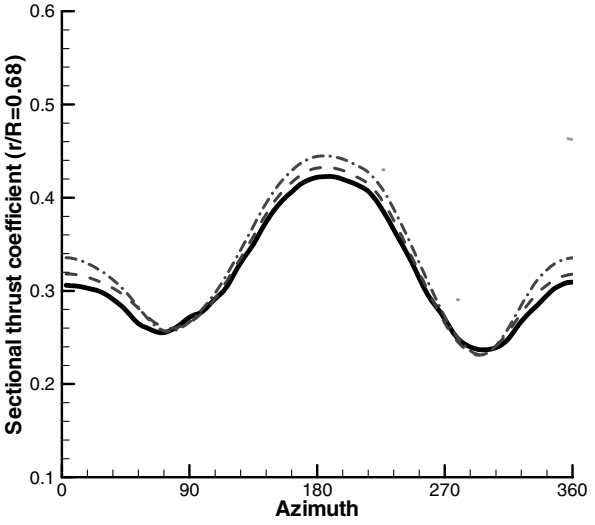

d) r/R=0.68

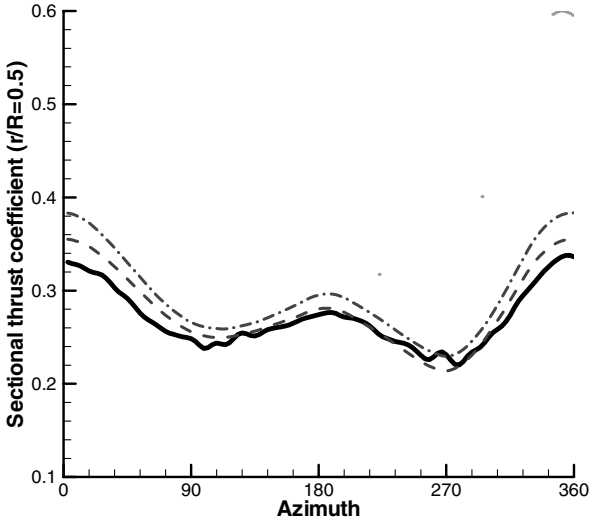

e) r/R=0.5

Fig. 11 Sectional loading coefficient ($M_{\text{Tip}} = 0.439$, $\mu = 0.05$).

predictor:

$$\mathbf{y}_p = \mathbf{y}_n + \frac{dt}{24}(55\mathbf{V}_n - 59\mathbf{V}_{n-1} + 37\mathbf{V}_{n-2} - 9\mathbf{V}_{n-3}) \quad (7)$$

corrector:

$$\mathbf{y}_{n+1} = \mathbf{y}_n + \frac{dt}{24}(9\mathbf{V}_p - 19\mathbf{V}_{n-1} + 5\mathbf{V}_{n-1} + \mathbf{V}_{n-2}) \quad (8)$$

where $\mathbf{y}_p$ is an intermediate position for the next position $\mathbf{y}_{n+1}$.

B. Tightly Coupled Computational Fluid Dynamics/Time-Marching Free-Wake Analysis

The rotor CFD is tightly coupled with the full-trailed TMFW. At each time step, a lifting line is obtained from the CFD calculation of the rotating blade. Then, this lifting line can make the trailed vortex filament of the free wake, using a relation between bounded vortices and trailed vortices. Using the lifting line and the Kutta–Joukowsky theory, the bound vortices' strength in the spanwise direction can be obtained, and the difference between the sectional bound vortices determines the trailed vortex strength at each time step:

$$\Gamma_{\text{bound}} = \text{lift}/(\rho V c); \qquad \Gamma_{\text{trailed}} = \Delta\Gamma_{\text{bound}} \quad (9)$$

where V is a sectional velocity and c is a chord length. The strength of the trailed vortices is used in a wake roll-up process of the TMFW. Figure 1 shows the position of the bound vortices and the motion of the trailed vortices. In the present study, the trailed vortices are placed at the trailing edge of the rotating blade. Moreover, one trailed vortex is matched with two CFD grids in a spanwise direction.

After the wake convection process, the TMFW gives an induced velocity field to the rotor CFD field. The induced velocity of the trailed vortices is used to correct the inflow and outflow conditions. The corrected condition provides a more accurate inflow rate near the rotor plane. In particular, hover and slow forward flight simulations are dependent on the inflow rate, considering the corrected boundary condition. This boundary correction approach is different from the conventional coupling approach. It is more effective in the unsteady computation, because the boundary correction approach is more robust and simple than the other coupling analysis. This process of coupling analysis is shown in Fig. 2.

After the computation of wake roll up, a wake sheet described by the trailed vortices is generated at each time step. Figure 3 shows that the wake sheet is directly connected to the rotating blade grid. The wake roll-up phenomenon is observed near the tip position, because the tip vortices are stronger than the inboard trailed vortices. Also, a distortion of the inboard wake sheet is investigated.

IV. Results and Discussion

In this section, hovering, slow forward, and forward flights were simulated. Specifically, hovering and slow forward simulations were tested in large (grid 1), medium (grid 2), and small (grid 3) background grids. Through the grid-size test, the coupled CFD/TMFW method proposed in this paper will be discussed. Additionally, the conventional rotor CFD was computed and compared with the coupled method.

A. Grid-Size Dependence in Hovering Flight

For the hovering case, the two-blade rotor was simulated using Caradonna and Tung's experimental rotor model with no taper and no twist [18]. At the tip Mach numbers 0.439 and 0.877, the computed results are compared with the experimental results.

The blade grid and the background grid are described in Figs. 4 and 5, respectively. The size of grid 1 is $10 \times 10 \times 10$ radius (total node number: 837,401). The medium-sized grid, grid 2, has a size of $4 \times 4 \times 4$ radius (total node number: 398,239). Grid 3 has the smallest size, which is $4 \times 4 \times 4$ radius (total node number: 337,737). The quality of all the grids is equal, because grids 2 and 3 are reduced from grid 1.

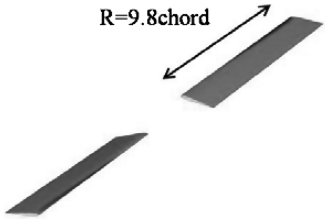

Fig. 12 AH-1G rotor model.

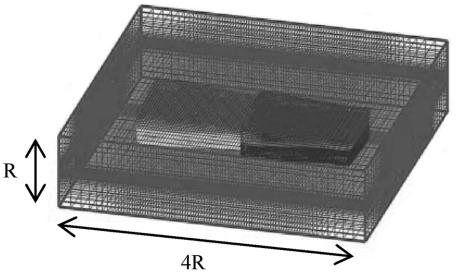

Fig. 13 Grid for the forward simulation.

In the tip Mach number 0.439, rotating blades with a pitch of 8 deg were calculated for 12 revolutions. The present coupled method's results were compared with results of the conventional inflow and outflow models, such as the source–sink condition and the Riemann-invariant condition (opening condition).

Table 1 shows the total thrust coefficient at each background grid. The sectional thrust coefficients of the present, the source–sink, and the Riemann-invariant conditions are compared at each background grid in Fig. 6. In Table 1 and Fig. 6, the results of the present coupled method can be seen to be almost the same as the results in grids 1, 2 and 3. However the results of the source–sink and the Riemann-invariant conditions diverge with grid-size reduction. This means that the present coupled method is more robust than those of the source–sink and the Riemann-invariant conditions.

The pressure coefficients of grid 3 are illustrated in Fig. 7. In the results of grid 3, the source–sink and the Riemann-invariant conditions failed to predict an aerodynamic loading on the surface of the rotating blades. Because the source–sink condition is derived from the fully developed one-dimensional theory, it cannot be used in grid 3. Moreover, the Riemann-invariant condition cannot describe the rotor wake out of the computational domain. The present method can only be applicable to grid 3.

The rotor was simulated at the transonic region as well as the subsonic region. At tip Mach number 0.877, the rotor blade rotates with a pitch angle of 8 deg. The total thrust coefficients are compared in Table 2. In these flow conditions, the results of the coupled method are better than those of the source–sink and the Riemann-invariant conditions. In the background of grid 3, the present method can be applicable. The sectional thrust coefficients are illustrated in Fig. 8. The present results in Fig. 8 are more reasonable than other results. Figure 9 shows the pressure coefficients in grid 3. In grid 3, the present results correspond only with the experimental data. Using the comparison between the present and the other results, it is found that the present method can be used generally with small as well as large grids.

B. Slow Forward Flight

Because the source–sink model is not available in the forward flight condition, the Riemann-invariant (opening) condition or the

Table 4 Cyclic control angle

Unit: degree	θ_0	θ_{1s}	θ_{1c}	β_{1s}	β_{1c}
Experiment	6	1.7	−5.5	2.13	−0.15
Present	6.2	1.38	−5.19	2.13	−0.15
Chung	6.1	1.4	−5.6	2.13	−0.15
Yang	8	2.5	−6.5	2.13	−0.15

present coupled approach should be used for prediction of the forward flight. In a large grid, the Riemann-invariant and the present inflow and outflow conditions could be applied. However, in a small grid, the Riemann-invariant condition would fail, due to its absence of a far wake.

For comparison between the present and the Riemann-invariant conditions, slow forward flight without flapping and pitching was simulated. A hovering model with a pitch angle of 8 deg and an advance ratio 0.05 was used for slow forward flight.

In Fig. 10, the wake structure during slow forward flight, described by the free-wake analysis, is shown. The average thrust coefficients are compared in Table 3. The thrust coefficients of the Riemann-invariant condition increase when the grid size decreases. Figure 11 shows the sectional thrust coefficients with the azimuth angle at the specific span positions. In this figure, a big difference in loading between the grids is shown in the inboard region. It seems that the inflow rate near the inboard is more sensitive, because the rotating velocity of the inboard is slower than the tip velocity.

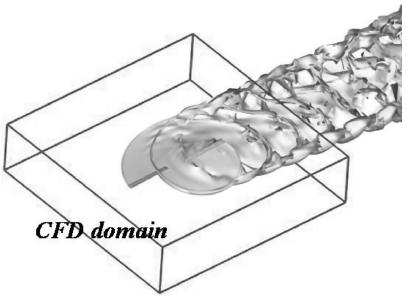

Fig. 14 Wake behaviors in the forward flight.

C. Forward Flight with Blade Motion

The rotating blades with cyclic pitch and flapping motions are simulated in forward flight. The rotor model is a two-blade model [19]. This model has an aspect ratio of 9.8, a linear twist of −10 deg, and symmetric airfoil. To avoid aeroelastic effects, a blade with a small aspect ratio is used. For blade motions, a trim analysis was conducted by controlling the cyclic pitch angle coefficients. The Newton–Rhapson iteration method is applied in the trim analysis for desired thrust and moment:

cyclic pith angle:

$$\theta(\psi) = \theta_0 + \theta_{1c}\cos(\psi) + \theta_{1s}\sin(\psi) \tag{10}$$

flapping angle:

$$\beta(\psi) = \beta_0 + \beta_{1c}\cos(\psi) + \beta_{1s}\sin(\psi) \tag{11}$$

The forward flight conditions are advance ratio 1.9 and rotational tip Mach number 0.65. Under these operation conditions, the average thrust coefficient is 0.00464. Figure 12 shows the rotor model used in the forward flight computation. The grid used in the computation is shown in Fig. 13. The CFD computation is only applied to the near field, and the inflow and outflow effects of the far field are considered using free-wake coupling. In Table 4, the cyclic pitching and the flapping angle coefficients are listed. The present control angle coefficients are compared with the results of the experiment by Chung et al. [20] and Yang et al. [21].

Figure 14 shows the wake behavior after free-wake computation. A wake distortion is shown from the advancing and retreating sides. After the rotor trimming, the sectional thrust variation with the azimuth angle is analyzed. In Fig. 15, the sectional thrusts at the specific span positions are shown. The present results are similar to the experimental data. In Fig. 15, the loading variation due to

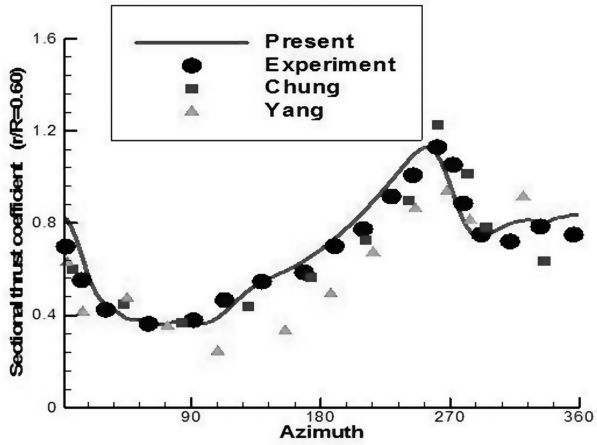

a) r/R=0.6

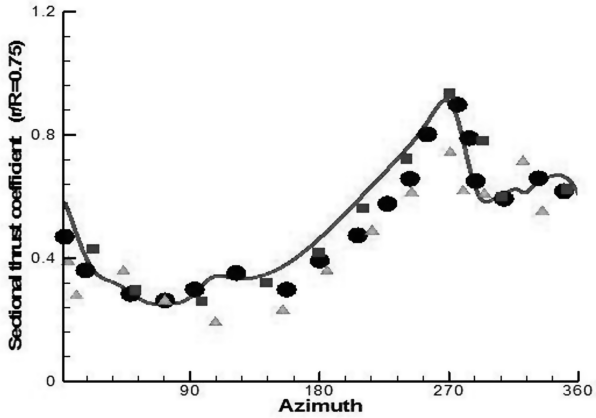

b) r/R=0.75

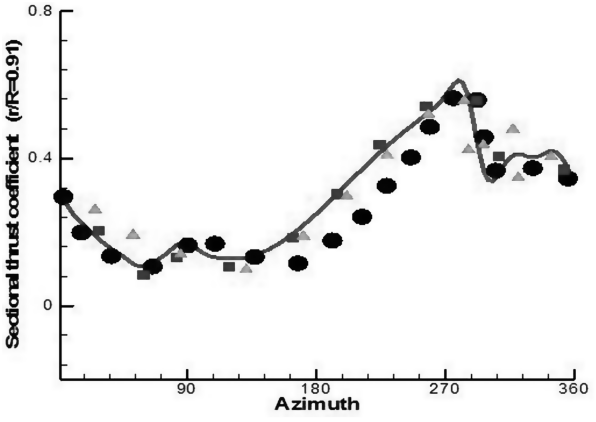

c) r/R=0.91

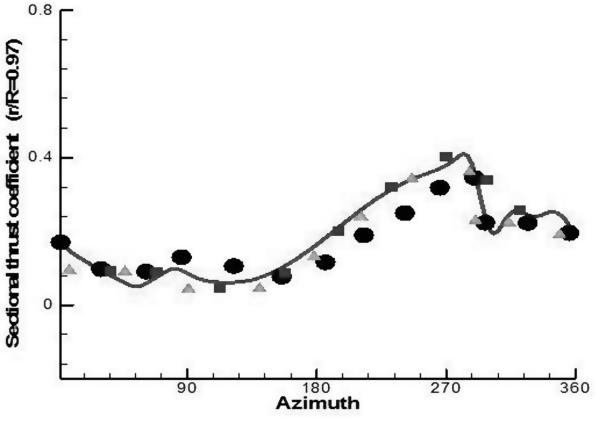

d) r/R=0.97

Fig. 15 Sectional thrust.

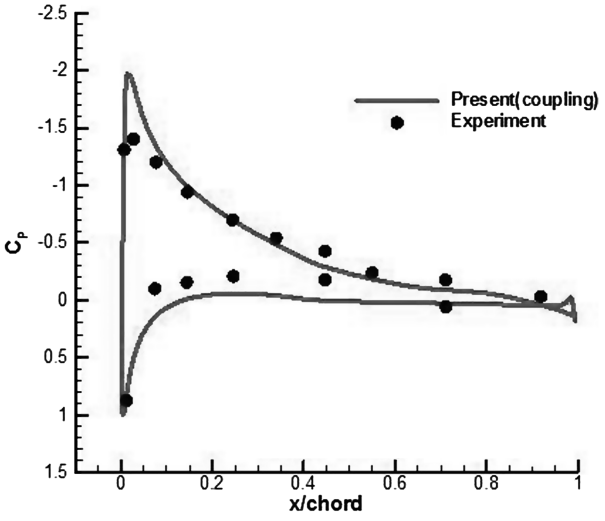

a) r/R=0.6, ψ=30°

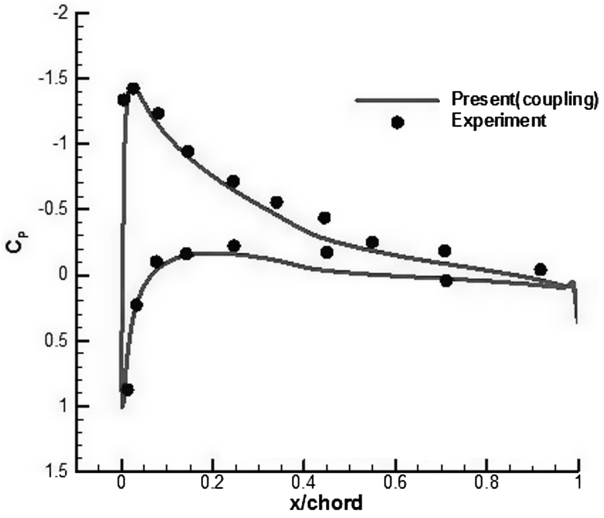

b) r/R=0.6, ψ=90

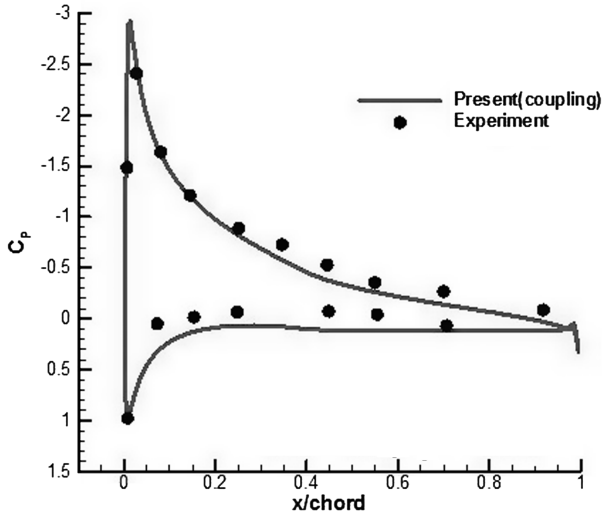

c) r/R=0.6, ψ=180°

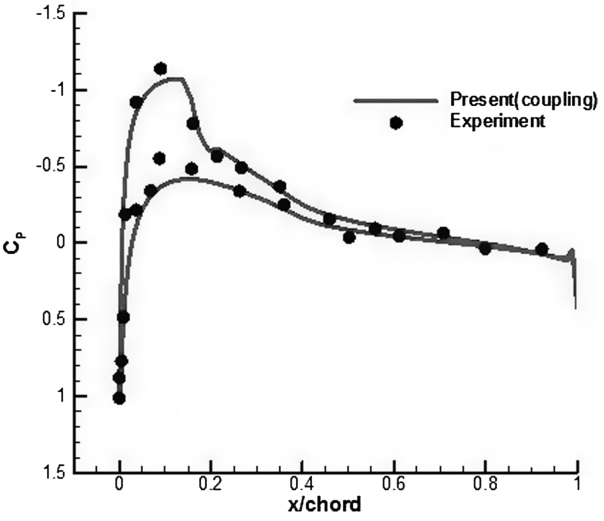

d) r/R=0.91, ψ=90

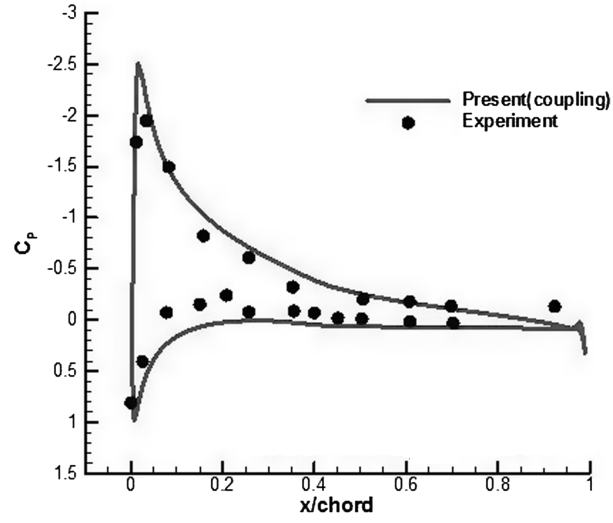

e) r/R=0.91, ψ=270°

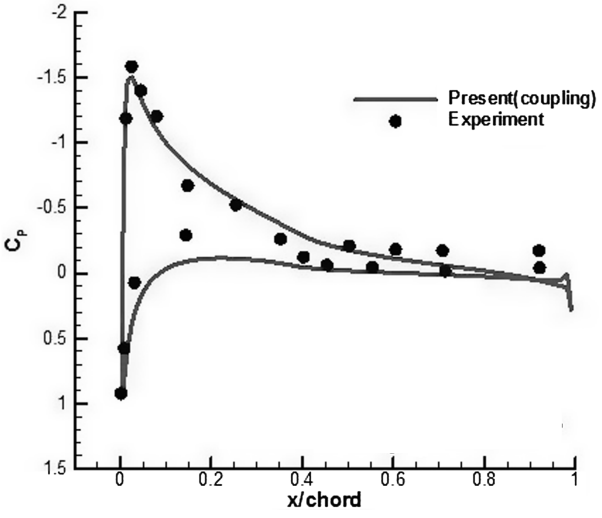

f) r/R=0.91, ψ=300°

Fig. 16 Pressure coefficients.

vortex interaction weakly occurs at an azimuth angle of 90 deg. Figure 16 shows the pressure coefficients at the specific azimuth and span positions. Figures 16a–16c are $r/R = 0.6$ results, and Figs. 16d–16f are $r/R = 0.91$ results. At $r/R = 0.91$ and an azimuth angle of 90 deg there is a local shock on the blade surface. Most of the results in Figs. 15 and 16 are in good accordance with the experimental data.

V. Conclusions

The present coupled method was applied to predict rotor aerodynamics. To investigate an advantage of the present method, not only large grids but small grids were used, and the present method was found to be applicable to small grids. The present method was applied to forward as well as hovering flight. The results were compared with the experimental data and showed good agreement. Here, the rotor aerodynamics computation is possible without a far-field grid, which means that the present coupled method is very robust and efficient.

The present method effectively describes the inflow and outflow induced by the wake structure. Furthermore, grid points can be intensively concentrated in the near field, because the far field grid is not necessary. If the blade–vortex interaction of the helicopter rotor is simulated, this method would be very useful, because blade vortex interaction (BVI) prediction generally requires huge computational resources. Moreover, this coupling approach can be widely used in other fields, such as wind turbines and airscrews.

Acknowledgments

This work was supported by the Defense Acquisition Program Administration (South Korea) and the Korean Agency for Defense Development under contract UD070041AD.

References

[1] Hariharan, N., and Sankar, L. N., "High-Order Essentially Nonoscillatory Schemes for Rotary-Wing Wake Computation," *Journal of Aircraft*, Vol. 41, No. 2, 2004, pp. 258–267. doi:10.2514/1.9320

[2] Dietz, M., Keßler, M., Krämer, E., and Wagner, S., "Tip Vortex Conservation on a Helicopter Main Rotor Using Vortex-Adapted Chimera Grids," *AIAA Journal*, Vol. 45, No. 8, 2007, pp. 2062–2074. doi:10.2514/1.28643

[3] He, C., and Zhao, J., "Modeling Rotor Wake Dynamics with Viscous Vortex Particle Method," 46th AIAA Aerospace Sciences Meeting and Exhibit, AIAA Paper 2008-338, 2008.

[4] Brown, R. E., "Rotor Wake Modeling for Flight Dynamic Simulation of Helicopters," *AIAA Journal*, Vol. 38, No. 1, 2000, pp. 57–63. doi:10.2514/2.922

[5] Berkman, M. E., and Sankar, L. N., "Navier–Stokes/Full Potential/Free-Wake Method for Rotor Flows," *Journal of Aircraft*, Vol. 34, No. 5, 1997, pp. 635–640. doi:10.2514/2.2240

[6] Schmitz, S., and Chattot, J., "A Coupled Navier–Stokes/Vortex-Panel Solver for the Numerical Analysis of Wind Turbines," *Computers and Fluids*, Vol. 35, No. 7, 2006, pp. 742–745. doi:10.1016/j.compfluid.2006.01.006

[7] Roe, P. L., "Approximate Riemann Solver, Parameter Vectors and Difference Schemes," *Journal of Computational Physics*, Vol. 43, No. 2, Oct. 1981, pp. 357–372. doi:10.1016/0021-9991(81)90128-5

[8] Harten, A., "High Resolution Schemes for Hyperbolic Conservation Laws," *Journal of Computational Physics*, Vol. 49, No. 3, 1983, pp. 357–393. doi:10.1016/0021-9991(83)90136-5

[9] Anderson, W. K., Tomas, J. L., and van Leer, B., "Comparison of Finite Volume Flux Vector Splittings for the Euler Equations," *AIAA Journal*, Vol. 24, No. 9, 1986, pp. 1453–1460. doi:10.2514/3.9465

[10] Pulliam, T., and Chaussee, D., "A Diagonal Form of an Implicit Approximate-Factorization Algorithm," *Journal of Computational Physics*, Vol. 39, No. 2, 1981, pp. 347–363. doi:10.1016/0021-9991(81)90156-X

[11] Park, S. H., Kim, Y., and Kwon, J. H., "Prediction of Damping Coefficients Using the Unsteady Euler Equations," *Journal of Spacecraft and Rockets*, Vol. 40, No. 3, 2003, pp. 356–362. doi:10.2514/2.3970

[12] Cho, K. W., Kwon, J. H., and Lee, S., "Development of a Fully Systemized Chimera Methodology for Steady/Unsteady Problems," *Journal of Aircraft*, Vol. 36, No. 6, 1999, pp. 973–980. doi:10.2514/2.2538

[13] Srinivasan, G. R., Raghavan, V., and Duque, E. P. N., "Flowfield Analysis of Modern Helicopter Rotors in Hover by Navier–Stokes Method," *Journal of the American Helicopter Society*, Vol. 38, No. 3, 1993, pp. 3–13.

[14] Strwan, R. C., and Djomehri, M. J., "Computational Modeling of Hovering Rotor and Wake Aerodynamics," *Journal of Aircraft*, Vol. 39, No. 5, 2002, pp. 786–793. doi:10.2514/2.3024

[15] Vatistas, G. H., Kozel, V., and Mih, W. C., "A Simpler Model for Concentrated Vortices," *Experiments in Fluids*, Vol. 11, No. 1, 1991, pp. 73–76. doi:10.1007/BF00198434

[16] Leishman, J. G., Baker, A., and Coyne, A. J., "Measurements of Rotor Tip Vortices Using Three-Component Laser Doppler Velocimetry," *Journal of the American Helicopter Society*, Vol. 41, No. 4, 1996, pp. 342–345. doi:10.4050/JAHS.41.342

[17] Cheney, W., and Kincaid, D., "Adams–Bashforth–Moulton Methods," *Numerical Mathematics and Computing*, 5th ed., Thomson Science, London, 2004, pp. 508–518.

[18] Caradonna, F. X., and Tung, C., "Experimental and Analytical Studies of a Model Helicopter Rotor in Hover," NASA TM-81232, 1982.

[19] Cross, J. L., and Watts, M. E., "Tip Aerodynamics and Acoustics Test: a Report and Data Survey," NASA Ames Research Center Rept. NASA-RP-1179, Moffett Field, CA, Dec. 1988.

[20] Chung, K. H., Hwang, C. J., Park, Y. M., Jeon, W. J., and Lee, D. J., "Numerical Predictions of Rotorcraft Unsteady Air-Loadings and BVI Noise by Using a Time-Marching Free-Wake and Acoustic Analogy," *Proceedings of the 31st European Rotorcraft Forum*, Royal Aeronautical Society, London, 2005.

[21] Yang, Z., Sankar, L. N., Smith, M. J., and Bauchau, O., "Recent Improvements to a Hybrid Method for Rotors in Forward Flight," *Journal of Aircraft*, Vol. 39, No. 5, 2002, pp. 804–812. doi:10.2514/2.3000